Research Article

Hard and tough novel high-pressure γ-Si₃N₄/Hf₃N₄ ceramic nanocomposites

Wei Li[a], Zhaoju Yu[b,*], Leonore Wiehl[a], Tianshu Jiang[a], Ying Zhan[a], Emmanuel III Ricohermoso[a], Martin Etter[c], Emanuel Ionescu[a,d], Qingbo Wen[e], Christian Lathe[c,f], Robert Farla[c], Dharma Teppala Teja[a], Sebastian Bruns[a], Marc Widenmeyer[a], Anke Weidenkaff[a,d], Leopoldo Molina-Luna[a], Ralf Riedel[a], Shrikant Bhat[c]

[a]*Department of Materials and Earth Sciences, Technical University of Darmstadt, Darmstadt 64283, Germany*
[b]*Key Laboratory of High Performance Ceramic Fibers (Xiamen University), Ministry of Education, College of Materials, Xiamen University, Xiamen 361005, China*
[c]*Deutsches Elektronen-Synchrotron DESY, Hamburg 22607, Germany*
[d]*Fraunhofer IWKS, Department Digitalization of Resources, Alzenau 63755, Germany*
[e]*State Key Laboratory of Powder Metallurgy, Central South University, Changsha 410083, China*
[f]*Deutsches GeoForschungsZentrum Potsdam, Potsdam 14473, Germany*

Abstract: Cubic silicon nitride (γ-Si₃N₄) is superhard and one of the hardest materials after diamond and cubic boron nitride (cBN), but has higher thermal stability in an oxidizing environment than diamond, making it a competitive candidate for technological applications in harsh conditions (e.g., drill head and abrasives). Here, we report the high-pressure synthesis and characterization of the structural and mechanical properties of a γ-Si₃N₄/Hf₃N₄ ceramic nanocomposite derived from single-phase amorphous silicon (Si)–hafnium (Hf)–nitrogen (N) precursor. The synthesis of the γ-Si₃N₄/Hf₃N₄ nanocomposite is performed at ~20 GPa and ca. 1500 ℃ in a large volume multi anvil press. The structural evolution of the amorphous precursor and its crystallization to γ-Si₃N₄/Hf₃N₄ nanocomposites under high pressures is assessed by the *in situ* synchrotron energy-dispersive X-ray diffraction (ED-XRD) measurements at ~19.5 GPa in the temperature range of ca. 1000–1900 ℃. The fracture toughness (K_{IC}) of the two-phase nanocomposite amounts ~6/6.9 MPa·m$^{1/2}$ and is about 2 times that of single-phase γ-Si₃N₄, while its hardness of ca. 30 GPa remains high. This work provides a reliable and feasible route for the synthesis of advanced hard and tough γ-Si₃N₄-based nanocomposites with excellent thermal stabililty.

Keywords: cubic silicon nitride (γ-Si₃N₄)/Hf₃N₄; ceramic nanocomposites; *in situ* synchrotron radiation; mechanical properties; thermal stability

* Corresponding author.
E-mail: zhaojuyu@xmu.edu.cn

1   Introduction

The high-pressure cubic silicon nitride (γ-Si$_3$N$_4$) phase possessing a spinel-type structure was first reported by Zerr *et al.* [1] in 1999. The spinel-type structure is characterized by one third of the silicon (Si) atoms being fourfold coordinated by nitrogen (N) atoms, and two thirds are sixfold coordinated by N atoms. The increase in the coordination number of silicon in γ-Si$_3$N$_4$ (as compared to that in α-/β-Si$_3$N$_4$) results in a significant increase in the density by 26%, which consequently results in a higher elastic modulus and hardness in comparison to those of the low-pressure hexagonal phases [2–6]. In addition, the high-temperature stability of γ-Si$_3$N$_4$ in an oxidizing environment is far beyond that of diamond [7,8]. Therefore, γ-Si$_3$N$_4$ is a potential candidate material for the application in harsh environments (e.g., drill head and abrasive). However, the major shortcoming of the γ-Si$_3$N$_4$ ceramic with respect to the above-mentioned applications relates to its low fracture toughness (K_{IC}), which is 3.5 MPa·m$^{1/2}$ [4]. The trade-off between hardness and fracture toughness in superhard materials makes it difficult to improve both properties simultaneously. For diamond and α-/β-Si$_3$N$_4$ systems, there are several promising methods to improve the toughness such as (nano)composite toughening, nanotwinning, and dislocation toughening. However, there has been little research on such approaches in γ-Si$_3$N$_4$.

Over the last few decades, the design of "ceramic nanocomposites" has been proven to be a highly effective method to improve the mechanical properties of ceramic materials at (ultra-)high temperatures [9–11]. The mechanical properties of TiN/Si$_3$N$_4$ and hafnium mononitride (HfN)/Si$_3$N$_4$ nanocomposites produced at ambient pressure conditions were significantly improved with the hardness of 25 and 19.6 GPa, respectively, due to the incorporation of TiN and HfN nanophase into the Si$_3$N$_4$ matrix (compared to ca. 16–17 GPa for α-/β-Si$_3$N$_4$) [12–14]. High-pressure-derived cubic Si$_3$N$_4$/Hf$_3$N$_4$ nanocomposites have not been reported yet. Due to the exceptional hardness of cubic γ-Si$_3$N$_4$, interesting mechanical properties of these composites can be expected. So far, there are only few reports on the mechanical properties of Hf$_3$N$_4$ as most of the research on Hf$_3$N$_4$ was focused on theory and the synthesis of films and powders instead of bulk materials. In general, besides appreciable mechanical properties, the preparation of bulk ceramic nanocomposites is extremely challenging. More precisely, the major issue is the restriction of grain growth during densification, which is often difficult by using conventional sintering techniques. In this study, the development and adoption of advanced processing techniques have been the subject of extensive research over the last few decades. High-pressure and high-temperature (HPHT) synthesis is one of the most suitable methods to prevent the recrystallization process and limit the grain growth owing to the reduced diffusion of atoms under high pressures and short holding time at the final synthesis temperature [15–17].

The polymer-derived ceramic (PDC) route has proven to be a promising method for the preparation of oxygen (O)-free and multielement ceramic nanocomposites [18,19]. As the polymeric single-source precursors can be tailored at the molecular level, final products with tunable chemical compositions and homogeneous elemental distributions can be consequently achieved. Moreover, the pyrolysis of the single-source precursors can be controlled to obtain amorphous or nanocrystalline materials at different temperatures [20], which provides access to metastable state compounds compared to other synthesis approaches. In consequence, the PDC route opens up a great opportunity to prepare novel ceramic nanocomposites with various compositions. Thus, single-phase amorphous SiMN ceramics (M being transition metals, e.g., Ti, hafnium (Hf), and V) as well as MN/α-Si$_3$N$_4$ and MN/β-Si$_3$N$_4$ ceramic nanocomposites were prepared starting from suitable metal-modified polysilazanes, which were ceramized and subsequently annealed at high temperatures [21,22].

In the present work, γ-Si$_3$N$_4$/Hf$_3$N$_4$ ceramic nanocomposites are prepared from an amorphous Si–Hf–N precursor using a large volume press (LVP). Furthermore, the phase evolution is studied *in situ* at HPHT conditions with the energy-dispersive X-ray diffraction (ED-XRD) using synchrotron radiation. These systematic studies allowed to determine the conditions for the formation and stability of the γ-Si$_3$N$_4$/Hf$_3$N$_4$ ceramic nanocomposites, which highlights the importance of using synchrotron beamlines to further investigate the transition behavior of stable and metastable ceramic nitride-based structures. The analysis of the mechanical properties proves that the resultant γ-Si$_3$N$_4$/Hf$_3$N$_4$ ceramic nanocomposite is a potential structural ceramic candidate material for industrial applications such as drill head and abrasives.

2 Experimental methods

2.1 Single-source-precursor synthesis and ammonolysis

The Hf-containing single-source precursor for the preparation of the SiHfN-based ceramic was synthesized upon the chemical modification of the commercial perhydropolysilazane (PHPS) solution (20 wt% of PHPS in dibutyl ether, Merck KGaA, Germany) by tetrakis (dimethylamido) hafnium(IV) (TDMAH; $\geq$ 99.99%, Sigma-Aldrich, Germany) with a weight ratio of TDMAH : PHPS = 30 : 70 [21]. Anhydrous toluene ($\geq$ 99.99%, Merck KGaA, Germany) was used as the reaction solvent. The synthesis of the single-source precursor was performed under an argon (Ar) atmosphere using the standard Schlenk technique. The synthesis process was carried out through the following steps: The brown and transparent solution of 1 g TDMAH dissolved in 5 mL anhydrous toluene was added dropwise into solution of 11.5 g PHPS (2.3 g pure PHPS) with constant stirring at room temperature for 6 h until a milky white gel-like reaction mixture was obtained. Then, the product was heated up to 50 ℃ for 2 h, followed by vacuum drying (10^{-2} mbar) for 5 h to remove the solvent and low-molecular-weight by-products, yielding a colorless solid precursor. The as-synthesized SiHfN precursor was ground and sieved in an Ar-filled glovebox (LABmaster pro, Mbraun, Germany) to avoid contamination with air and moisture. The sieved fine powders were placed in an alumina boat, and then transferred into a horizontal Schlenk tube under the protection of an Ar atmosphere. Afterwards, the tube was pumped three times under vacuum and refilled with high-purity ammonia (NH_3, > 99.98%, Air Liquide, France; $H_2O \leqslant$ 200 ppm) up to the atmospheric pressure. The sample was ammonolyzed at 1000 ℃ for 2 h at a heating rate of 50 ℃/h under a continuous flow of NH_3 (1.5 L/h), and then cooled down to room temperature at a rate of 60 ℃/h. The as-ammonolyzed specimen was used as raw material for the subsequent high-pressure experiments.

2.2 High-pressure synthesis including *in situ* ED-XRD

The HPHT experiments were carried out using a Hall-type six-ram LVP (mavo press LPQ6 1500-100, Max Voggenreiter GmbH, Germany) at the beamline P61B at DESY, Hamburg [23]. Tungsten carbide (WC) second-stage anvils (32 mm, FUJILLOY TF08, Japan) with a truncated edge length of 4 mm were used to compress a MgO octahedron with 10 mm edge length (Cr_2O_3-doped). The MgO octahedron assembly was used as a pressure transmitting medium along with an h-BN–TiB_2 cylindrical heater (EBN grade, Denka Japan, Japan). Further details about the assembly can be found in Ref. [23]. The obtained precursor powders were hand-pressed into a hole in a metal disc (height (h) = 1.4 mm, diameter (ϕ) = 1.8 mm) inside the glovebox, and then placed into an h-BN tube to avoid contact with air or moisture. The assembly was first compressed to the target pressure at room temperature, and then heated stepwise to the target temperature. Finally, the samples with dimensions between 0.5 and 1.8 mm in ϕ were obtained.

The HPHT *in situ* ED-XRD was used to investigate the crystallization behavior of the SiHfN ceramic. Prior to the experiments, the Ge-detector position was determined to be 5.009° using an LaB_6 standard (National Institute of Standards and Technology (NIST) SRM 660c), and the diffracted X-rays from the sample were collected in the energy range of 20–160 keV. The ED-XRD patterns were recorded during heating at different temperatures up to ca. 1900 ℃ (rounded— calculated values of ±20 ℃ based on a calibrated power-temperature relationship), after the temperature had reached a steady state during each heating step. The main phases were identified with the help of a program called PDIndexer [24]. The temperature dependence of the Si_3N_4 and Hf_3N_4 lattice parameters was determined by the peak profile fitting using the program General Structure Analysis System (GSAS)-II [25].

The *in situ* ED-XRD was also used to monitor the pressure in real time inside the octahedron assembly using the MgO pressure marker (run #BT448, 19.5± 0.5 GPa). In order to investigate the mechanical properties of the obtained γ-Si_3N_4/Hf_3N_4 ceramic nanocomposites, an additional synthesis experiment was carried out without X-rays at a calibrated pressure and temperature (run #HH547, ~20 GPa and ca. 1500 ℃). The sample recovered in run #HH547 was used for further characterizations.

2.3 Characterization

The synthesis and the crosslinking processes of the single-source precursors were analyzed *ex situ* by the Fourier transform infrared (FTIR) spectroscopy on a spectrometer (Varian 670-IR, Agilent Technologies,

USA), using the attenuated total reflection (ATR) mode in the range of 500–4000 cm^{-1}. The high-resolution angle-dispersive X-ray diffraction (AD-XRD) of the recovered samples was performed at the high-energy beamline P02.1 (60 keV, λ = 0.207 Å) of PETRA III, DESY, Hamburg. The quantitative phase analysis was made by the Rietveld refinements, using the program GSAS-II [25]. The instrumental profile parameters were calibrated with an LaB$_6$ standard material. The surface of the recovered sample was coated with gold for the measurements of the microstructure and chemical composition by a scanning electron microscope (SEM; XL30 FEG, FEI Company, Hillsboro, Oregon, USA) equipped with an energy-dispersive detector. The Vickers indentation and cracks were measured by the SEM coupled with the energy dispersive spectrometer (JSM 7600F, JEOL Ltd., Japan). The acceleration voltage was 15 kV. The carbon (C) and N/O contents of the SiHfN ceramic pyrolyzed at 1000 ℃ were measured by the analyzers (LECO C-200, LECO Instrumente GmbH, Germany, and LECO TC-436, LECO Instrumente GmbH, Germany, respectively). The contents of Si and Hf were analyzed by the energy-dispersive spectroscopy (EDS). The lamella for the transmission electron microscopy (TEM)/scanning transmission electron microscopy (STEM) measurements was prepared using a focused ion beam (FIB) instrument (JIB-4600F, JEOL, Japan). To investigate the microstructure of the recovered sample (#HH547), the bright-field transmission electron microscopy (BFTEM) images (some are also at high resolutions, HR-TEM) were acquired along with the selected area electron diffraction (SAED) patterns using a transmission electron microscope (JEM-ARM200F, JEOL, Japan). The acceleration voltage was 200 kV.

The nanohardness and Young's modulus (E) were measured by an iNano device (Nanomechanics Inc., Oak Ridge, TN, USA) under a load of 50 mN. Nine random indentations were performed on the polished surface (Table S2 in the Electronic Supplementary Material (ESM)). The Vickers hardness (HV) of the polished sample was measured for each applied load (F) from 0.49 to 48 N by a diamond indenter (FV-700B, Future-Tech, Japan), and the loading time was kept at 15 s. At least five indentations were repeated and averaged to ensure the reliability of the results. The K_{IC} was calculated from the indentation crack (c) and impression diagonal (a) using the Anstis [26] and Evans equation [27] (Eqs. (1) and (2), respectively):

$$K_{IC-Anstis} = 0.016F(E/HV)^{0.5}/c^{1.5} \quad (1)$$

$$K_{IC-Evans} = 0.16HVa^2/c^{1.5} \quad (2)$$

The thermal stability was measured by a thermogravimetric analysis (TGA) device (STA 449F3 Jupiter, NETZSCH, Germany) in purified compressed air (gas purifier removes CO$_2$, H$_2$O, and hydrocarbons to ppb range) from room temperature to 1300 ℃ for 1 h at the heating rate of 5 ℃/min. The same device was used for measurements to investigate the pyrolysis process under flowing NH$_3$ (10 vol% Ar in NH$_3$). All measurements were corrected for the buoyancy.

3 Results and discussion

3.1 Single-source-precursor synthesis and pyrolysis

The perhyropolysilazane chemically-modified with TDMAH was investigated by the FTIR spectroscopy. The FTIR spectra of the dried pristine PHPS and TDMAH as well as the synthesized precursor and the obtained amorphous SiHfN ceramic are shown in Fig. 1. The absorption bands at 3372 and 1171 cm^{-1} (N–H), 2137 cm^{-1} (Si–H), and 840–1030 cm^{-1} (Si–N–Si) are characteristics for the dried pure PHPS. The FTIR spectrum of unreacted TDMAH exhibits typical C–H absorption bands at 2766, 2822, and 2948 cm^{-1}. The absorption bands at 932 and 1251 cm^{-1} are assigned to the Hf–N–C vibrations [28]. The intensity of the N–H and Si–H absorption bands of the PHPS decreases after the chemical modification, indicating that the reaction
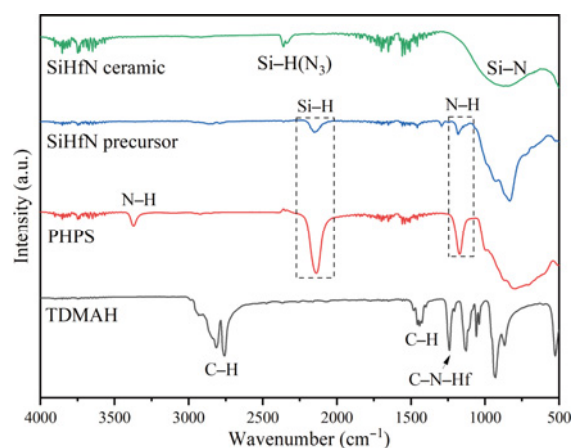
Fig. 1 FTIR spectra of TDMAH, dried PHPS, SiHfN precursor, and SiHfN ceramic obtained after pyrolysis of precursor at 1000 ℃ in NH$_3$.

with TDMAH occurred at the Si–H/N–H groups of PHPS. Based on Refs. [28,29] and our previous work [21], PHPS with the Hf-modified N–H and Si–H bonds leads to the formation of N–Hf at N centers and Si–Hf linkages, which is accompanied by the release of HNMe$_2$ and CH$_4$. The absorption peaks of the N–H and Si–H bands completely vanish after pyrolysis at 1000 ℃, and asymmetric stretching vibrations of Si–N (800–950 cm^{-1}) [30] and Si–H(N$_3$) (2300 cm^{-1}) [31,32] are observed, which indicate that the complete polymer-to-ceramic transformation has been achieved.

The ceramic yield of the SiHfN ceramic pyrolyzed at 1000 ℃ under NH$_3$ is as high as 97.9 wt% (Fig. S1 in the ESM). The elemental analysis of the as-obtained SiHfN ceramic revealed compositions of Si (49.68± 3.16 wt%), Hf (14.77±2.72 wt%), N (33.51±3.84 wt%), O (2.03±0.46 wt%), and C (0.01 wt%), demonstrating that the Hf-modified PHPS leads to a significant increase in the N content in comparison with the pure PHPS (ca. 25 wt%). The Si : Hf molar ratio of the pyrolyzed SiHfN ceramic amounts ca. 21 : 1, which is close to the molar ratio used for the synthesis of the SiHfN precursor (18 : 1). According to the elemental analysis data, the empirical formula of our material amounts Si$_{1.0}$Hf$_{0.05}$N$_{1.35}$O$_{0.07}$. By neglecting the O content, the composition of the nanocomposite is estimated to be 20 : 1 γ-Si$_3$N$_4$/Hf$_3$N$_4$. According to Ref. [22], the modification of PHPS with TDMAH is limited in the SiHfN system due to steric hindrance, which results in a slightly higher Si content in the

pyrolyzed SiHfN ceramic. In addition, the XRD pattern (Fig. S2 in the ESM) reveals that the as-obtained SiHfN ceramic is X-ray amorphous. Therefore, it has to be considered that during the subsequent HPHT treatment of the amorphous SiHfN ceramic, polymorphic transitions will occur to form α-Si$_3$N$_4$, β-Si$_3$N$_4$, and γ-Si$_3$N$_4$, as well as HfN and Hf$_3$N$_4$.

3. 2 Structural evolution of SiHfN ceramic at HPHT

A selection of the ED-XRD patterns recorded at 19.5(±0.5) GPa and at different temperatures in the range from room temperature to approximately 1900 ℃ is shown in Fig. 2(a). At ca. 1000 ℃, only intense fluorescence lines of Hf and Pb (from detector shielding materials) were observed, indicating that no crystalline phase is formed in the amorphous SiHfN ceramic up to this temperature, which is in agreement with our XRD results of the synthesized amorphous SiHfN ceramic (Fig. S2 in the ESM).

Starting at ca. 1100 ℃, the Bragg reflections of γ-Si$_3$N$_4$ and Th$_3$P$_4$-type Hf$_3$N$_4$ appear and grow in intensity on further heating. In addition, some reflections of β-Si$_3$N$_4$ are visible at the beginning, which disappear on further heating. Under these conditions, β-Si$_3$N$_4$ transforms into the stable γ-phase. There are no further structural changes in the XRD patterns up to ca. 1550 ℃, which reveals that the γ-Si$_3$N$_4$/Hf$_3$N$_4$ composite is thermodynamically stable up to ca. 1550 ℃. In addition, the lattice parameters of Th$_3$P$_4$-type Hf$_3$N$_4$
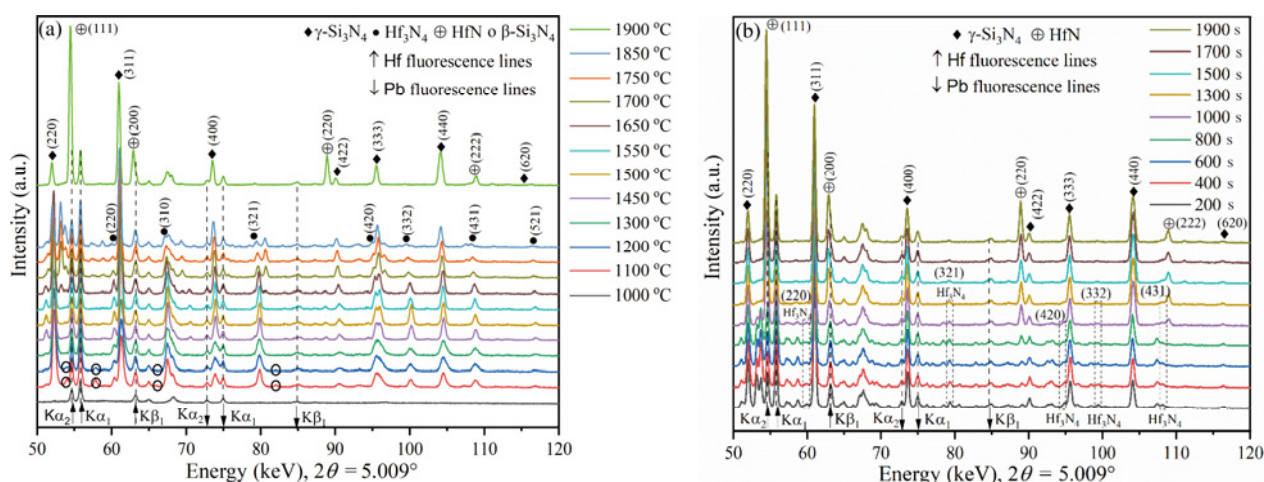
Fig. 2 Sequence of ED-XRD patterns, showing phase transformation in SiHfN ceramic at 19.5(±0.5) GPa: (a) on heating in temperature range of ca. 1000–1900 ℃ rounded to ±20 ℃, including some β-Si$_3$N$_4$ reflections (the hollow circle) visible at ~1100 ℃ (the red line) and with reduced intensity at ~1200 ℃ (the blue line), namely (101) 54 keV, (120) 58 keV, (210) 66 keV, and (301) 82 keV. (b) On holding maximum temperature of ca. 1900 ℃ during time range between 200 and 1900 s, HfN phase appears, best visible by HfN (220) and (222) reflections.

and γ-Si₃N₄ were refined from the reflection positions by using the peak-fitting routine of GSAS-II and are shown in Fig. S4 and Table S1 in the ESM. Based on this observation, the synthesis conditions of around ca. 1500 ℃ and ~20 GPa are selected to prepare a γ-Si₃N₄/Hf₃N₄ ceramic nanocomposite in an additional experiment (#HH547). This sample is used for further analysis of the microstructure and mechanical properties.

Above this temperature, some new reflections appear and gradually strengthen with the increasing temperature up to ca. 1900 ℃, best visible in Fig. 2(a) in the energy range between γ-Si₃N₄ (220) at ~52 keV and the Hf Kα₂ fluorescence line at 54.6 keV. This intermediate phase coexists with γ-Si₃N₄ and Th₃P₄-type Hf₃N₄ in the temperature interval from ca. 1650 to 1900 ℃. The growth of the intermediate phase partly, however not fully, consumes the Hf₃N₄ phase, visible in Fig. 2(a) by the decreasing intensity of the Hf₃N₄ reflections. Only after ~15 min of relaxation time at ca. 1900 ℃, Hf₃N₄ and the intermediate phase vanish together and are replaced by HfN (Fig. 2(b)). The growth of HfN can be best judged from the HfN (220) and (222) reflections at ~89 and ~109 keV, respectively, which are clearly visible in Fig. 2(b). The ED-XRD patterns of the sample after quenching the temperature at high pressures and after decompression indicate that the phase transition of Hf₃N₄ into rocksalt HfN is irreversible. An additional XRD measurement (Fig. S3 in the ESM) of the recovered sample (#BT448) shows a mixture of γ-Si₃N₄ and HfN and only a tiny fraction of remaining Hf₃N₄ (0.1 wt%). The refined phase fractions show a Si₃N₄ : HfN weight ratio of 7.1 : 1, corresponding to an atomic ratio of Si : Hf = 29 : 1, similar to the result from elemental analysis of the precursor (Si : Hf = 21 : 1).

The analyzed phase evolution of amorphous SiHfN under HPHT conditions is illustrated by the compositional phase diagram, as shown in Fig. 3. Accordingly, the amorphous SiHfN phase separates
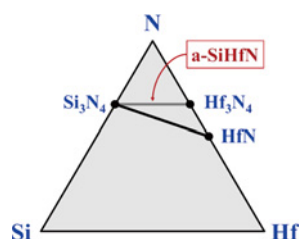
Fig. 3 Thermodynamic guideline for synthesis of high-pressure nitride nanocomposites in ternary SiHfN system.

along the tie line into γ-Si₃N₄ and Hf₃N₄ at ~20 GPa and ca. 1100 ℃. At temperature far beyond ca. 1550 ℃, Hf₃N₄ decomposes along the tie line into rock salt-type HfN and N₂ according to Reaction (3), which is then in thermodynamic equilibrium with γ-Si₃N₄.

$$2Hf_3N_4 \rightarrow 6HfN + N_2 \qquad (3)$$
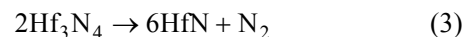
3.3 Characterization of γ-Si₃N₄/Hf₃N₄ composite

3.3.1 AD-XRD

An AD-XRD powder pattern of the recovered sample #HH547 was measured by synchrotron radiation. The Rietveld refinements (Fig. 4) show essentially two phases, namely γ-Si₃N₄ and Hf₃N₄ and some small reflections of a yet unidentified third phase, resulting in a residual of *wR* = 9.6%. In addition, there are reflections from the capsule material c-BN, which could not be completely separated from the sample. The refined phase fractions show a Si₃N₄ : Hf₃N₄ weight ratio of 8.93 : 1, from which the atomic ratio of Si : Hf = 38 : 1 was calculated. This value is larger than the result from the elemental analysis of the precursor (Si : Hf = 21 : 1), suggesting that the unknown third phase is rich in Hf.

3.3.2 TEM

The BFTEM images and SEM–EDS analysis of the resultant γ-Si₃N₄/Hf₃N₄ ceramic nanocomposite synthesized at ~20 GPa and ca. 1500 ℃ are shown in Fig. 5 and Fig. S5 in the ESM, respectively. Figure 5(a) indicates that the Hf₃N₄ grains/particles identified by the significant darker contrast are homogeneously dispersed in the γ-Si₃N₄ matrix. The microstructure of the γ-Si₃N₄/Hf₃N₄ ceramic nanocomposite has been
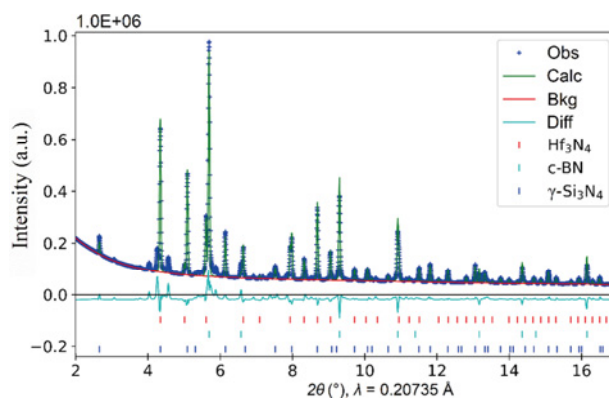
Fig. 4 Rietveld refinements (*wR* = 9.6%) of γ-Si₃N₄/ Hf₃N₄ composite, recovered from HPHT experiment at ~20 GPa and ca. 1500 ℃.

studied through the BFTEM images and SAED patterns, as shown in Figs. 5(b) and 5(c), to identify the two phases. The SAED pattern with the [001] zone axis in Fig. 5(b) shows the face-centered cubic lattice of the large γ-Si$_3$N$_4$ single crystal visible in the image, and two representative reflections, i.e., (4 0 0) and (2 $-$2 0), are denoted in the SAED pattern. The corresponding lattice spacings are 0.193 and 0.274 nm. The SAED image taken from the whole region in

Fig. 5(c) exhibits a polycrystalline aggregate composed of Hf$_3$N$_4$ and γ-Si$_3$N$_4$. Furthermore, in the HR-TEM images (Figs. 5(e) and 5(f)), the (311) lattice plane of γ-Si$_3$N$_4$ and the (211) lattice plane of Hf$_3$N$_4$ are also identified by the *d* spacings of 0.233 and 0.274 nm, respectively. In addition, the existence of Hf$_3$N$_4$ in the γ-Si$_3$N$_4$ matrix can also be clearly seen in Figs. 5(c)–5(f). In Fig. 5(f), dispersed Hf$_3$N$_4$ nanocrystallites are embedded in micron-sized Si$_3$N$_4$ particles.
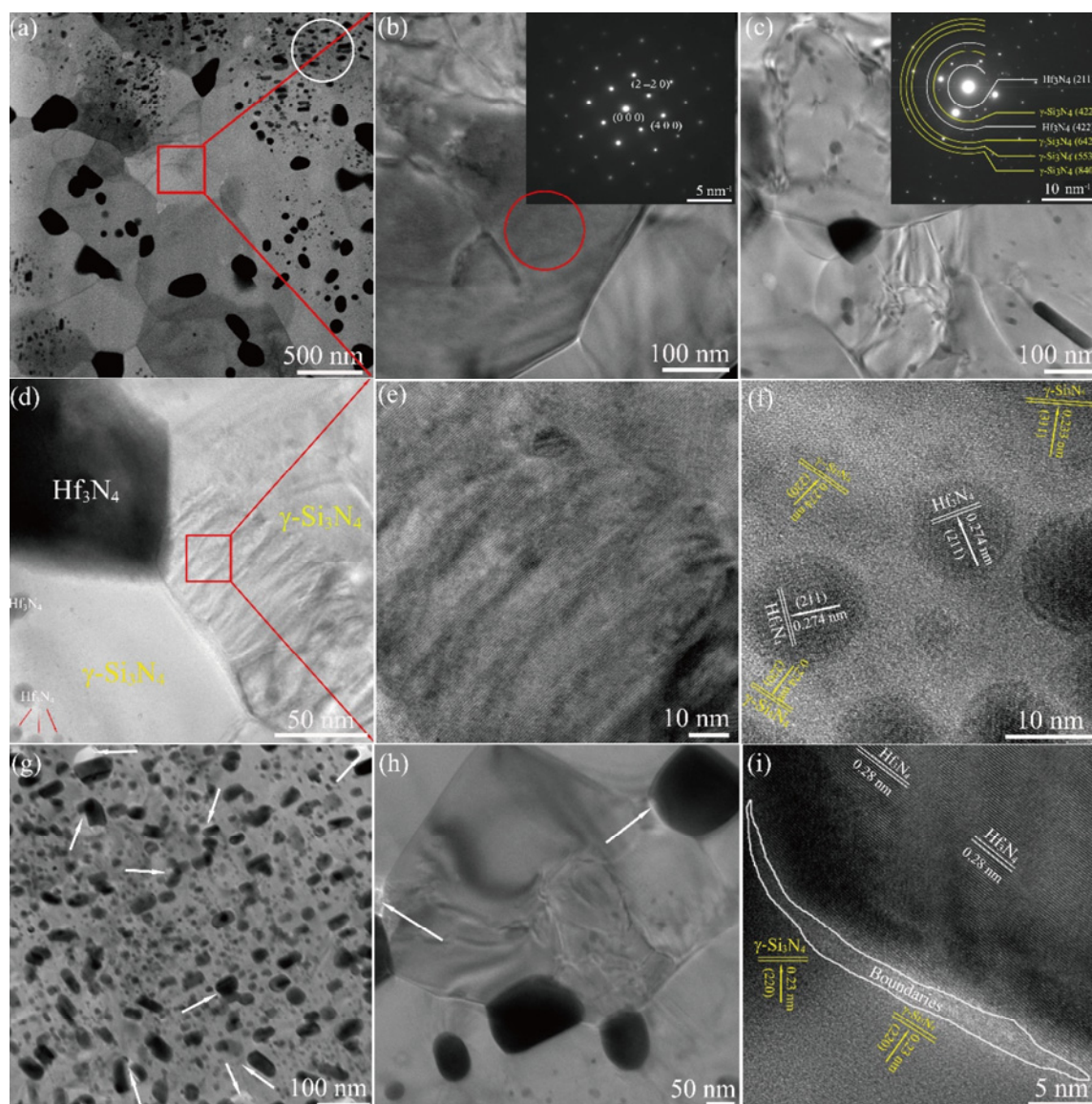
Fig. 5 BFTEM images of γ-Si$_3$N$_4$/Hf$_3$N$_4$ nanocomposite synthesized at ~20 GPa and ca. 1500 ℃: (a) BFTEM image of typical microstructure of γ-Si$_3$N$_4$/Hf$_3$N$_4$ nanocomposite; (b) BFTEM image acquired from (a) (the inset is the SAED image taken from the red box region); (c) BFTEM image and corresponding SAED image (the inset is the raw data in Fig. S6 in the ESM); (d) BFTEM image showing interface between Hf$_3$N$_4$ and γ-Si$_3$N$_4$ crystals; (e) HR-TEM micrograph magnified from the red box area in (d), showing lattice fringes from imperfect γ-Si$_3$N$_4$ single crystal with some embedded nanospheres of Hf$_3$N$_4$; (f) Hf$_3$N$_4$ nanoparticles embedded in γ-Si$_3$N$_4$. (g) BFTEM image obtained from the white circled area in (a), and the white arrows point at the nanopores; (h) HR-TEM image showing interaction relationship between γ-Si$_3$N$_4$, Hf$_3$N$_4$ nanograins, and nanopores; and (i) HR-TEM micrograph magnified from the interphase area.

Furthermore, nanopores and an amorphous interphase between Hf_3N_4 and γ-Si_3N_4 were obverved, as shown in Figs. 5(g)–5(i). The presence of nanopores and interphase has a significant impact on the mechanical properties, which will be discussed in conjunction with the fracture toughness.

3.3.3 Mechanical properties

In order to show a potential application of the γ-Si_3N_4/ Hf_3N_4 ceramic as a hard and tough material, the mechanical properties of the ceramic composite were measured. The nanohardness and E were analyzed by the nanoindentation technique. The nanohardenss and E are 42±1 and 574±33 GPa (the detailed values are shown in Table S2 in the ESM), respectively, which are comparable to the hardness of pure γ-Si_3N_4 [3,33] and comparable to those of commercial superhard materials such as polycrystalline diamond [34] and cubic boron nitride (cBN) [35]. The Vickers hardness and fracture toughness of the γ-Si_3N_4/Hf_3N_4 nanocomposites were measured at indentation loads from 0.49 to 48 N on a polished surface. As can be seen in Fig. 6, the Vickers hardness and the fracture toughness of γ-Si_3N_4/Hf_3N_4 decrease with the increasing load. Although the Vickers hardness of Hf_3N_4 (18.7 GPa) [36] is lower than that of the superhard γ-Si_3N_4 (43 GPa) [33], an average high hardness value of 28±2 GPa for the γ-Si_3N_4/Hf_3N_4 nanocomposite is achieved at $F = 9.8$ N, which is comparable to the Vickers hardness of stishovite SiO_2 (33 GPa) [37,38] and γ-Ge_3N_4 (28 GPa) [39], and is
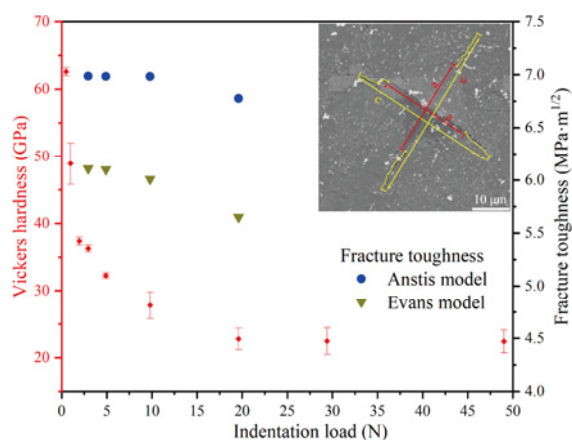
Fig. 6 Vickers Hardness and fracture toughness of γ-Si_3N_4/Hf_3N_4 nanocomposite as a function of indentation load in the range of 0.49–48 N (the detailed values are shown in Table S3 in the ESM). The inset is a representative SEM indentation image showing cracks under an indentation load of 19.6 N.

much higher than those of the experimental and theoretical hardness values of Hf_3N_4 [36] and other transition metal nitrides such as Zr_3N_4 [36,40], NbN [41], γ-MoN [42], HfN [41], and ZrN [41].

The fracture toughness (Fig. 6) of the γ-Si_3N_4/Hf_3N_4 ceramic nanocomposite is estimated based on the relation between indentation load and the radius/length of cracks (Fig. S7 in the ESM). The fracture toughness decreases with the increasing indentation load, showing an average value of ~6.9±0.5 MPa·$m^{1/2}$ in the Anstis equation (Eq. (1)) and ~6.0±0.6 MPa·$m^{1/2}$ in the Evans equation (Eq. (2)), far exceeding that of pure γ-Si_3N_4 (3.5 MPa·$m^{1/2}$), as reported in Ref. [4]. In order to identify the potential mechanisms accounting for the enhanced toughness of γ-Si_3N_4/Hf_3N_4 ceramic, the radial cracks generated by the Vickers indentation were further characterized. The representative SEM images of the indentation and radial cracks are shown in Fig. 7. The black and white areas in Fig. 7 correspond to γ-Si_3N_4 and Hf_3N_4, respectively, which can also be seen from the EDS mappings of Fig. S5 in the ESM. The radial cracks show the micro-/nano-sized zigzag propagation paths and crack bridging (Figs. 7(b)–7(d)), and the obvious intergranular/transgranular fracture mode is found when the crack meets the Hf_3N_4 grains [43]. Moreover, the typical BFTEM image of the resultant γ-Si_3N_4/Hf_3N_4 ceramic reveals some Hf_3N_4 nanograins with sizes in the range of ~10–100 nm (Figs. 5(g) and 5(h)) in the γ-Si_3N_4 matrix. Nano-sized Hf_3N_4 particles contribute to crack deflection, resulting in energy dissipation of the fracture process, and thereby enhancing the fracture toughness [44]. Figure 5(g) is a BFTEM image of the sample, in which some irregular nanopores with a size ranging from 20 to 100 nm are distributed at the interphase triple junctions (Fig. 5(h)). Traditionally, porosity and weak interface are considered detrimental to mechanical properties [45], especially in brittle ceramics, as both can initiate catastrophic failure at low-stress levels. However, the presence of nanopores and amorphous interphase in the matrix can enhance the fracture toughness as the sizes of the nanopores are much smaller than the critical crack size of γ-Si_3N_4/Hf_3N_4 ceramic, and the initiated microcracks are blunted by the nanopore-mediated interphase [46]. Furthermore, the nanopores provide free space to accommodate interphase plastic strain by eliminating the nanopores [46]. In addition, the analyzed transgranular and intergranular fracture modes are
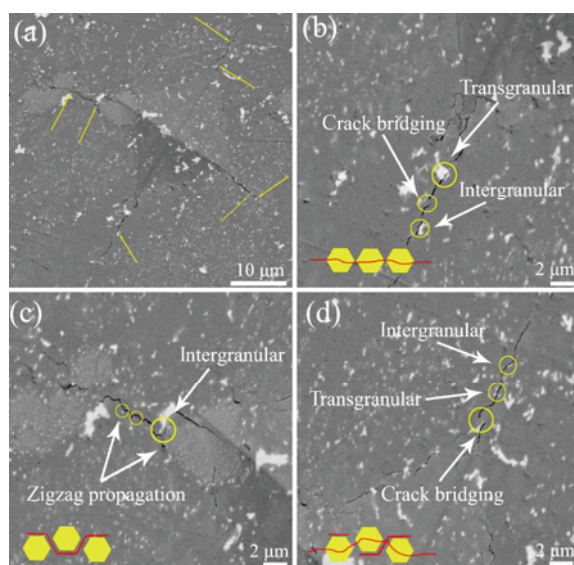
Fig. 7 SEM images of indentation and cracks at 9.8 N. In (a), the yellow arrows indicate the transgranular cracks. In (b–d), the path of crack propagation is schematically described (the hexagons show the grain, and the red color represents the crack).

considered to be dependant on the chemistry of the formed amorphous interphase in our γ-Si_3N_4/Hf_3N_4 ceramic composites. In summary, the presence of nano-sized grains and nanoporosity are discussed as the origin for the analyzed increase in the fracture toughness [46,47].

In order to comprehensively evaluate the Vickers hardness and the fracture toughness of the γ-Si_3N_4/ Hf_3N_4 nanocomposite, a comparison with other hard materials is compiled and shown in Fig. 8 [3,4,16, 33,48–63]. It is obvious that most hard materials show low fracture toughness, and only few of them (WC and α-/β-Si_3N_4) also exhibit high K_{IC}. Accordingly, the resultant γ-Si_3N_4/Hf_3N_4 ceramic composite exhibits both high hardness and fracture toughness simultaneously, which is an excellent trade-off between hardness and fracture toughness compared to most other hard materials. Therefore, the high-pressure γ-Si_3N_4/Hf_3N_4 nanocomposite is considered to be a potential candidate material for cutting tool applications.

3.3.4 Thermal stability

The thermal stability of the as-preapred γ-Si_3N_4/Hf_3N_4 nanocomposite was characterized by a TGA/ differential thermal analysis (DTA) measurement in air at a heating rate of 5 ℃/min. Jiang *et al.* [7] reported that the phase transformation of γ-Si_3N_4 to α-Si_3N_4 takes place in air at 1400–1600 ℃; therefore, in

order to avoid the phase transition, the measurement of thermal stability was performed at 1300 ℃ for 1 h. As shown in the TGA/DTA curves (Fig. 9), there are four steps for the oxidation progress. The first onset oxidation temperature of the γ-Si_3N_4/Hf_3N_4 nanocomposite is 780 ℃, which is higher than those of nanograined diamond (~680 ℃) [16] and natural diamond (770 ℃) [64], but lower than those of nanotwinned diamond (980 ℃) [64] and nano cBN (1090 ℃) [16]. Beyond 780 ℃, the γ-Si_3N_4/Hf_3N_4 ceramic nanocomposite shows a continuous mass gain, which is considered to be due to the reaction of the
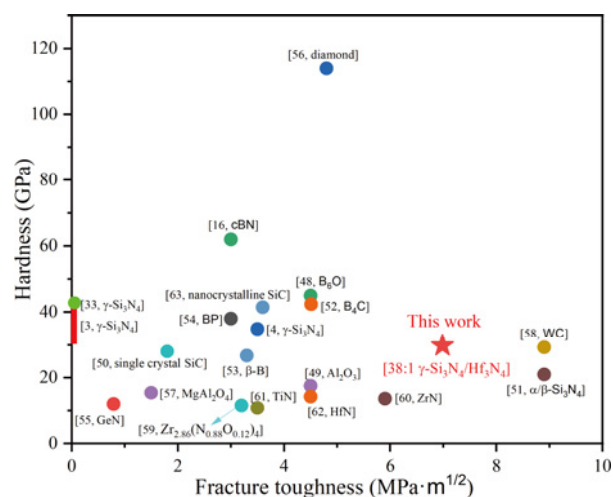
Fig. 8 HV and K_{IC} of γ-Si_3N_4/Hf_3N_4 nanocomposite (load: 9.8 N) in comparison with those of the reported hard materials (38 : 1 is the calculated composition of the nanocomposite by the Rietveld refinements. References [3,33] only show hardness but no fracture toughness; the loads used in the respective hardness measurements are detailed in Table S3 in the ESM).
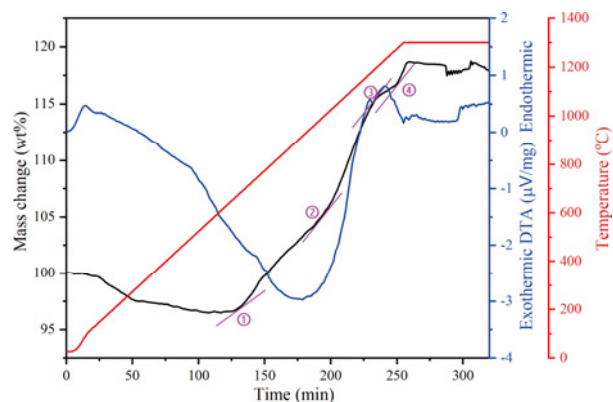
Fig. 9 TG (the black line), DTA (the blue line), and temperature (the red line) curves of γ-Si_3N_4/Hf_3N_4 nanocomposite in air. ①, ②, ③, and ④ represent the onset oxidation temperatures.

Si–N and Hf–N bonds with air to form the Si–O and Hf–O bonds. The mass change up to 1300 ℃ after holding for 1 h amounts ca. 18 wt% and is much less than those for nanotwinned diamond at 1100 ℃ (75 wt%) [64], diamond/c-BN composite at 1100 ℃ (80 wt%) [65], nano diamond at 1000 ℃ (45 wt%) [16], and natural diamond at 850 ℃ (87.5 wt%) [64] and is finally stabilized at that temperature. The Si– and Hf–oxide layers formed by the oxidation of the γ-Si_3N_4/Hf_3N_4 nanocomposite prevent further oxidation compared with the oxidation of diamond to continuously form CO/CO_2 [64,66].

4   Conclusions

Within the present work, the phase transformation of amorphous SiHfN ceramic prepared by the PDC route under HPHT conditions is investigated by means of the synchrotron XRD measurements. The results provide clear guidance for the preparation of high-pressure γ-Si_3N_4/Hf_3N_4 and γ-Si_3N_4/HfN ceramic nanocomposites. Based on the *in situ* XRD analysis, the γ-Si_3N_4/Hf_3N_4 ceramic nanocomposite is obtained at ~1500 ℃ and ~20 GPa. At temperatures beyond 1500 ℃ under the same pressure, the Hf_3N_4 phase decomposes to HfN, and a γ-Si_3N_4/HfN nanocomposite is formed.

The fracture toughness of the resultant γ-Si_3N_4/Hf_3N_4 ceramic nanocomposite (~6/6.9 MPa·m$^{1/2}$) exhibits a significant improvement over pure γ-Si_3N_4 (3.5 MPa·m$^{1/2}$) without sacrificing the hardness of the material. Characterizations by means of the XRD, SEM, and TEM proved that the enormous enhancement in the fracture toughness has to be discussed in terms of synergetic effects of nano-scale composite (γ-Si_3N_4 $\leqslant$ 200 nm and Hf_3N_4 $\leqslant$ 50 nm), nanopores, and transgranular fracture mode. In addition to the unique combination of high hardness and high toughness, the γ-Si_3N_4/Hf_3N_4 nanocomposite exhibits relatively high thermal stability, which can be operated in extreme environments and at elevated temperatures.

Declaration of competing interest

The authors have no competing interests to declare that are relevant to the content of this article.

Electronic Supplementary Material

Supplementary material is available in the online version of this article at https://doi.org/10.26599/JAC.2023.9220764.

References

[1] Zerr A, Miehe G, Serghiou G, *et al*. Synthesis of cubic silicon nitride. *Nature* 1999, **400**: 340–342.

[2] Zerr A, Riedel R, Sekine T, *et al*. Recent advances in new hard high-pressure nitrides. *Adv Mater* 2006, **18**: 2933–2948.

[3] Zerr A, Kempf M, Schwarz M, *et al*. Elastic moduli and hardness of cubic silicon nitride. *J Am Ceram Soc* 2002, **85**: 86–90.

[4] Nishiyama N, Ishikawa R, Ohfuji H, *et al*. Transparent polycrystalline cubic silicon nitride. *Sci Rep* 2017, **7**: 44755.

[5] Boyko TD, Hunt A, Zerr A, *et al*. Electronic structure of spinel-type nitride compounds Si_3N_4, Ge_3N_4, and Sn_3N_4 with tunable band gaps: Application to light emitting diodes. *Phys Rev Lett* 2013, **111**: 097402.

[6] Nishiyama N, Langer J, Sakai T, *et al*. Phase relations in silicon and germanium nitrides up to 98 GPa and 2400 ℃. *J Am Ceram Soc* 2019, **102**: 2195–2202.

[7] Jiang JZ, Kragh F, Frost DJ, *et al*. Hardness and thermal stability of cubic silicon nitride. *J Phys-Condens Mat* 2001, **13**: L515–L520.

[8] Tallant DR, Parmeter JE, Siegal MP, *et al*. The thermal stability of diamond-like carbon. *Diam Relat Mater* 1995, **4**: 191–199.

[9] Palmero P. Structural ceramic nanocomposites: A review of properties and powders' synthesis methods. *Nanomaterials* 2015, **5**: 656–696.

[10] Mukhopadhyay A, Basu B. Consolidation–microstructure–property relationships in bulk nanoceramics and ceramic nanocomposites: A review. *Int Mater Rev* 2007, **52**: 257–288.

[11] Yue YH, Gao YF, Hu WT, *et al*. Hierarchically structured diamond composite with exceptional toughness. *Nature* 2020, **582**: 370–374.

[12] Bechelany MC, Proust V, Gervais C, *et al*. *In situ* controlled growth of titanium nitride in amorphous silicon nitride: A general route toward bulk nitride nanocomposites with very high hardness. *Adv Mater* 2014, **26**: 6548–6553.

[13] Kumar A, Gokhale A, Ghosh S, *et al*. Effect of nano-sized sintering additives on microstructure and mechanical properties of Si_3N_4 ceramics. *Mater Sci Eng A* 2019, **750**: 132–140.

[14] Li W, Li F, Yu ZJ, *et al*. Polymer-derived SiHfN ceramics: From amorphous bulk ceramics with excellent mechanical properties to high temperature resistant ceramic nanocomposites. *J Eur Ceram Soc* 2022, **42**: 4493–4502.

[15] Suffner J, Scherer T, Wang D, *et al*. Microstructure and high-temperature deformation behavior of Al_2O_3–TiO_2 obtained from ultra-high-pressure densification of metastable powders. *Acta Mater* 2011, **59**: 7592–7601.

[16] Solozhenko VL, Kurakevych OO, Le Godec Y. Creation of nanostuctures by extreme conditions: High-pressure synthesis of ultrahard nanocrystalline cubic boron nitride. *Adv Mater* 2012, **24**: 1540–1544.

[17] Melaibari AA, Zhao JN, Molian P, *et al*. Ultrahard boron nitride material through a hybrid laser/waterjet based surface treatment. *Acta Mater* 2016, **102**: 315–322.

[18] Colombo P, Mera G, Riedel R, *et al*. Polymer-derived ceramics: 40 years of research and innovation in advanced ceramics. *J Am Ceram Soc* 2010, **93**: 1805–1837.

[19] Yuan J, Hapis S, Breitzke H, *et al*. Single-source-precursor synthesis of hafnium-containing ultrahigh-temperature ceramic nanocomposites (UHTC-NCs). *Inorg Chem* 2014, **53**: 10443–10455.

[20] Ionescu E, Terzioglu C, Linck C, *et al*. Thermodynamic control of phase composition and crystallization of metal-modified silicon oxycarbides. *J Am Ceram Soc* 2013, **96**: 1899–1903.

[21] Zhou C, Gao X, Xu Y, *et al*. Synthesis and high-temperature evolution of single-phase amorphous Si–Hf–N ceramics. *J Eur Ceram Soc* 2015, **35**: 2007–2015.

[22] Zhou C. Ternary Si–metal–N ceramics: Single-source-precursor synthesis, nanostructure and properties characterization. Ph.D. Thesis. Darmstadt, Germany: Technical University of Darmstadt, 2017.

[23] Farla R, Bhat S, Sonntag S, *et al*. Extreme conditions research using the large-volume press at the P61B endstation, PETRA III. *J Synchrotron Radiat* 2022, **29**: 409–423.

[24] Seto Y. PDIndexer 2022. https://github.com/seto77/PDIndexer/.

[25] Toby BH, Von Dreele RB. GSAS-II: The genesis of a modern open-source all purpose crystallography software package. *J Appl Crystallogr* 2013, **46**: 544–549.

[26] Anstis GR, Chantikul P, Lawn BR, *et al*. A critical evaluation of indentation techniques for measuring fracture toughness: I, Direct crack measurements. *J Am Ceram Soc* 1981, **64**: 533–538.

[27] Evans AG, Charles EA. Fracture toughness determinations by indentation. *J Am Ceram Soc* 1976, **59**: 371–372.

[28] Li KJ, Li SG, Li N, *et al*. Tetrakis(dimethylamido)hafnium adsorption and reaction on hydrogen terminated Si(100) surfaces. *J Phys Chem C* 2010, **114**: 14061–14075.

[29] Iwamoto Y, Kikuta KI, Hirano SI. Synthesis of poly-titanosilazanes and conversion into Si_3N_4–TiN ceramics. *J Ceram Soc Jpn* 2000, **108**: 350–356.

[30] Lucovsky G, Yang J, Chao SS, *et al*. Nitrogen-bonding environments in glow-discharge—Deposited a-Si:H films. *Phys Rev B* 1983, **28**: 3234–3240.

[31] Mazzarella L, Kolb S, Kirner S, *et al*. Optimization of PECVD process for ultra-thin tunnel SiO_x film as passivation layer for silicon heterojunction solar cells. In: Proceedings of the 2016 IEEE 43rd Photovoltaic Specialists Conference, Portland, USA, 2016: 2955–2959.

[32] Günthner M, Wang KS, Bordia RK, *et al*. Conversion behaviour and resulting mechanical properties of polysilazane-based coatings. *J Eur Ceram Soc* 2012, **32**: 1883–1892.

[33] Tanakaa I, Oba F, Sekine T, *et al*. Hardness of cubic silicon nitride. *J Mater Res* 2002, **17**: 731–733.

[34] Li GX, Rahim MZ, Pan WC, *et al*. The manufacturing and the application of polycrystalline diamond tools—A comprehensive review. *J Manuf Process* 2020, **56**: 400–416.

[35] Monteiro SN, Skury ALD, de Azevedo MG, *et al*. Cubic boron nitride competing with diamond as a superhard engineering material—An overview. *J Mater Res Technol* 2013, **2**: 68–74.

[36] Mattesini M, Ahuja R, Johansson B. Cubic Hf_3N_4 and Zr_3N_4: A class of hard materials. *Phys Rev B* 2003, **68**: 184108.

[37] Stishov S M, Popova S V. New dense polymorphic modification of silica. *Geokhimiya* 1962, **8**: 649–659.

[38] Léger JM, Haines J, Schmidt M, *et al*. Discovery of hardest known oxide. *Nature* 1996, **383**: 401.

[39] Shemkunas MP, Petuskey WT, Chizmeshya AVG, *et al*. Hardness, elasticity, and fracture toughness of polycrystalline spinel germanium nitride and tin nitride. *J Mater Res* 2004, **19**: 1392–1399.

[40] Dzivenko D. High-pressure synthesis, structure and properties of cubic zirconium(IV)- and hafnium(IV) nitrides. Ph.D. Thesis. Darmstadt, Germany: Technical University of Darmstadt, 2009.

[41] Wang SM, Antonio D, Yu XH, *et al*. The hardest superconducting metal nitride. *Sci Rep* 2015, **5**: 13733.

[42] Chen XJ, Struzhkin VV, Wu ZG, *et al*. Hard superconducting nitrides. *PNAS* 2005, **102**: 3198–3201.

[43] Zhao J, Ai X, Lv ZJ. Preparation and characterization of Si_3N_4/TiC nanocomposite ceramics. *Mater Lett* 2006, **60**: 2810–2813.

[44] Cao MR, Wang SB, Han WB. Influence of nanosized SiC particle on the fracture toughness of ZrB_2-based nanocomposite ceramic. *Mater Sci Eng A* 2010, **527**: 2925–2928.

[45] Krstic VD. Porosity dependence of strength in brittle solids. *Theor Appl Fract Mec* 1988, **10**: 241–247.

[46] Madhav Reddy K, Guo JJ, Shinoda Y, *et al*. Enhanced mechanical properties of nanocrystalline boron carbide by nanoporosity and interface phases. *Nat Commun* 2012, **3**: 1052.

[47] Madhav Reddy K, Guo DZ, Lahkar S, *et al*. Graphite interface mediated grain-boundary sliding leads to enhanced mechanical properties of nanocrystalline silicon carbide. *Materialia* 2019, **7**: 100394.

[48] He DW, Zhao YS, Daemen L, *et al*. Boron suboxide: As hard as cubic boron nitride. *Appl Phys Lett* 2002, **81**: 643–645.

[49] Auerkari P. *Mechanical and Physical Properties of Engineering Alumina Ceramics*. Espoo, Finland: Valtion teknillinen tutkimuskeskus, 1996.

[50] Qian J, Daemen LL, Zhao Y. Hardness and fracture toughness of moissanite. *Diam Relat Mater* 2005, **14**: 1669–1672.

[51] Filgueira M, Nascimento ÁLN, Oliveira MP, *et al*. HPHT sintering of binderless Si_3N_4: Structure, microstructure, mechanical properties and machining behavior. *J Braz Soc Mech Sci* 2018, **40**: 118.

[52] Wang CC, Song LL. Nanosheet-structured B_4C with high hardness up to 42 GPa. *Chin Phys B* 2019, **28**: 066201.

[53] Qin JQ, Nishiyama N, Ohfuji H, *et al*. Polycrystalline γ-boron: As hard as polycrystalline cubic boron nitride. *Scripta Mater* 2012, **67**: 257–260.

[54] Gui R, Xue Z, Zhou XF, *et al*. Strain stiffening, high load-invariant hardness, and electronic anomalies of boron phosphide under pressure. *Phys Rev B* 2020, **101**: 035302.

[55] Drory MD, Ager JW III, Suski T, *et al*. Hardness and fracture toughness of bulk single crystal gallium nitride. *Appl Phys Lett* 1996, **69**: 4044–4046.

[56] Novikov NV, Dub SN. Fracture toughness of diamond single crystals. *J Hard Mater* 1992, **2**: 5–11.

[57] Morita K, Kim BN, Hiraga K, *et al*. Fabrication of high-strength transparent $MgAl_2O_4$ spinel polycrystals by optimizing spark-plasma-sintering conditions. *J Mater Res* 2009, **24**: 2863–2872.

[58] Ma DJ, Kou ZL, Liu YJ, *et al*. Sub-micron binderless tungsten carbide sintering behavior under high pressure and high temperature. *Int J Refract Met H* 2016, **54**: 427–432.

[59] Dzivenko DA, Zerr A, Miehe G, *et al*. Synthesis and properties of oxygen-bearing c-Zr_3N_4 and c-Hf_3N_4. *J Alloys Compd* 2009, **480**: 46–49.

[60] Alexandre N, Desmaison-Brut M, Valin F, *et al*. Mechanical properties of hot isostatically pressed zirconium nitride materials. *J Mater Sci* 1993, **28**: 2385–2390.

[61] Moriyama M, Aoki H, Kobayashi Y, *et al*. The mechanical properties of hot-pressed TiN ceramics with various additives. *J Ceram Soc Jpn* 1993, **101**: 279–284.

[62] Desmaison-Brut M, Montintin J, Valin F, *et al*. Mechanical properties and oxidation behaviour of HIPed hafnium nitride ceramics. *J Eur Ceram Soc* 1994, **13**: 379–386.

[63] Sun RX, Wei XD, Hu WT, *et al*. Nanocrystalline cubic silicon carbide: A route to superhardness. *Small* 2022, **18**: 2201212.

[64] Huang Q, Yu DL, Xu B, *et al*. Nanotwinned diamond with unprecedented hardness and stability. *Nature* 2014, **510**: 250–253.

[65] Liu YJ, He DW, Kou ZL, *et al*. Hardness and thermal stability enhancement of polycrystalline diamond compact through additive hexagonal boron nitride. *Scripta Mater* 2018, **149**: 1–5.

[66] Li W, Du HZ, Tian CM, *et al*. Single-source-precursor derived bulk Si_3N_4/HfB_xN_{1-x} ceramic nanocomposites with excellent oxidation resistance. *Z Anorg Allg Chem* 2022, **648**: e202200203.